

Tunable spin helical Dirac quasiparticles on the surface of three-dimensional HgTe

Chang Liu,^{1,2} Guang Bian,¹ Tay-Rong Chang,³ Kedong Wang,² Su-Yang Xu,¹ Ilya Belopolski,¹ Irek Miotkowski,⁴ Helin Cao,⁴ Koji Miyamoto,⁵ Chaoqiang Xu,⁶ Christian E. Matt,⁷ Thorsten Schmitt,⁷ Nasser Alidoust,¹ Madhab Neupane,¹ Horng-Tay Jeng,³ Hsin Lin,⁸ Arun Bansil,⁹ Vladimir N. Strocov,⁷ Mark Bissen,¹⁰ Alexei V. Fedorov,¹¹ Xudong Xiao,^{6,12} Taichi Okuda,⁵ Yong P. Chen,⁴ and M. Zahid Hasan¹

¹Joseph Henry Laboratory and Department of Physics, Princeton University, Princeton, New Jersey 08544, USA

²Department of Physics, South University of Science and Technology of China, Shenzhen, Guangdong 518055, China

³Department of Physics, National Tsing Hua University, Hsinchu 30013, Taiwan

⁴Department of Physics, Purdue University, West Lafayette, Indiana 47907, USA

⁵Hiroshima Synchrotron Radiation Center, Hiroshima University, 2-313 Kagamiyama, Higashi-Hiroshima 739-0046, Japan

⁶Department of Physics, The Chinese University of Hong Kong, Hong Kong, China

⁷Swiss Light Source, Paul Scherrer Institut, CH-5232 Villigen, Switzerland

⁸Graphene Research Centre and Department of Physics, National University of Singapore, Singapore 117542

⁹Department of Physics, Northeastern University, Boston, Massachusetts 02115, USA

¹⁰Synchrotron Radiation Center, University of Wisconsin-Madison, 3731 Schneider Drive, Stoughton, Wisconsin 53589, USA

¹¹Advanced Light Source, Lawrence Berkeley National Laboratory, Berkeley, California 94305, USA

¹²Center for Photovoltaics and Solar Energy, Shenzhen Institutes of Advanced Technology, Chinese Academy of Sciences, Shenzhen, China

(Received 7 December 2014; revised manuscript received 30 July 2015; published 22 September 2015)

We show with systematic photoemission spectroscopy and scanning tunneling spectroscopy data that a spin helical surface state appears on the (110) surface of noncentrosymmetric, three-dimensional HgTe. The topological surface state in HgTe exhibits sharp, linear dispersion without k_z variation, as well as clear, left-right imbalanced spin polarization and circular dichroism. Chemical gating by alkali metal deposition on the surface causes the unexpected opening and/or increase of a surface insulating gap without changing its topological property. Such an unusual behavior we uncover in three-dimensional HgTe sheds light on a convenient control of the Fermi surface and quantum transport in a topological insulator.

DOI: [10.1103/PhysRevB.92.115436](https://doi.org/10.1103/PhysRevB.92.115436)

PACS number(s): 71.70.Ej, 03.65.Vf, 68.35.Rh, 79.60.-i

I. INTRODUCTION

Mercury telluride (HgTe) and several related II-VI materials have been widely accepted as zero or negative gap semiconductors [1–4]. Studies of HgTe in its size-confined state (HgTe-CdTe quantum wells) mark the experimental realization of a topological insulator (TI), one of the most important discoveries in condensed matter physics in the past decade [5–13]. As a decisive spectroscopic signature for identifying a TI, the helical spin-momentum locking behavior of the topological surface states (TSSs) have been observed experimentally in prototypical systems such as $\text{Bi}_{1-x}\text{Sb}_x$ and $\text{Bi}_2(\text{Se},\text{Te})_3$, where the spin component tangential to the band contours shows opposite polarization on opposite sides of a Dirac cone surface state [12,14,15]. Regarding HgTe, scientific interest and potential applications have thus far been limited to confined structures such as strained thin films and nanoscaled hybrid quantum wells where a two-dimensional (2D), quantum spin Hall insulator is realized [5,16–18]. Interestingly, it is theoretically found that *bulk* HgTe exhibits *three-dimensional* (3D) topologically nontrivial behaviors that are special in at least two aspects. First, it exhibits topological nontriviality without spatial inversion symmetry. Such noncentrosymmetric topological systems have recently been brought to broad scientific attention [19–21], as exotic ground-state electronic structures are expected by allowing a nonzero Rashba-type bulk antisymmetric spin-orbit coupling term. Second, an unrelated band (the lower part of the Γ_8 band) is found to span across the energy inverted topological gap in HgTe [17,18], rendering the system semimetallic with surface Dirac fermions

masked by bulk valence electrons at all energy levels. A 3D topological insulating state appears only when external strain breaks the four-fold crystallographic symmetry and opens a full insulating gap [22]. In this paper, we show with systematic data from spin resolved and circular dichroic angle-resolved photoemission spectroscopy (ARPES) that a single Dirac cone TSS exists on the surface of 3D HgTe crystals whose Dirac point energy is located very close to the Fermi level. Despite the energy degeneration with a holelike bulk electron sea at all energies, the topological Dirac quasiparticles of HgTe exhibit sharp, linear dispersion without visible k_z variation, as well as clear, left-right imbalanced spin polarization and circular dichroism that is comparable in degree with an in-gap Dirac cone. Our first-principles calculation not only proves unambiguously the topological nontrivial nature of the linear band but also exhibit excellent agreement on the degree of its spin polarization. Further band calculations with surface atomic relaxation taken into account indicates the presence of a sizable gap between the upper and lower parts of the Γ_8 band in the surface of as-grown HgTe crystals. Our scanning tunneling spectroscopy (STS) dI/dV curve shows no contradiction with this hypothesis. The size of this surface gap is further found to be increasing with increasing deposition of alkali metals (K and Cs) onto the surface. Such unusual tunability we uncover in three-dimensional HgTe sheds light on controlling the conductivity and electronic mobility of a topological insulator in an accurate and convenient manner. The present study opens the door for extensive spectroscopic and transport research on this topologically nontrivial system

without inversion symmetry, and paves the way for topological devices based on this widely-studied bulk material without size confinement.

II. MATERIALS AND METHODS

HgTe single crystals were grown in a vertical Bridgman apparatus. Growth takes place in simple 2-zone furnaces with the pure elements contained in thick-walled high-purity quartz ampoules. The thick ampoule walls (3–4 mm) are needed to contain the high (up to ~ 60 atm) mercury vapor pressures within the ampoules with increasing temperature up to 700 °C for direct synthesis from elements. For this purpose, an improved ampoule seal-off procedure was developed to make the growth at the higher temperatures possible. Both Hg and Te of 6N commercial purity were purified further via multiple vacuum distillations in a high purity quartz designs operating under dynamic vacuum of 10^{-8} torr. The distillation procedures significantly reduced the amount of Cu and/or Ag acting as acceptors. The single crystal range of existence for mercury telluride in the Hg-Te binary system is almost completely on the tellurium side. The maximum mercury nonstoichiometry in single crystals of HgTe grown from the melt is expected to be $1.7 \times 10^{-5}\%$ at. To assure high-quality materials, the growth rates used during Bridgman growth were about 0.2–0.4 mm/hour.

Ultraviolet spin integrated ARPES measurements were performed at Beamline 4.0.3 (MERLIN) and 10.0.1 (HERS) of the Advanced Light Source (ALS), and Beamline 5-4 of the Stanford Synchrotron Radiation Lightsource (SSRL), California, USA, using VG-Scienta R8000 and R4000 electron analyzers with incident photon energies ranging from 18 to 60 eV. Soft x-ray spin integrated ARPES experiments were performed at the ADDRESS beamline at the Swiss Light Source, Villigen, Switzerland, with incident photon energies ranging from 310 to 700 eV (Ref. [23]). Spin-resolved ARPES measurements were performed at the ESPRESSO end station installed at Beamline-9B of the Hiroshima Synchrotron Radiation Center (HiSOR), Hiroshima, Japan, equipped with state-of-the-art very low-energy electron diffraction (VLEED) spin detectors utilizing preoxidized Fe(001)-p(1 × 1)-O targets [24] (detailed in Ref. [25], with additional Refs. [26–35]). The two spin detectors are placed at an angle of 90° and are directly attached to a VG-Scienta R4000 hemispheric analyzer, enabling simultaneous spin resolved ARPES measurements for all three spin components as well as high-resolution spin integrated ARPES experiments. Circular dichroic ARPES measurements were performed at the APPLE-PGM Beamline at the Synchrotron Radiation Center (SRC), Stoughton, Wisconsin, as well as Beamline 12.0.1 of the ALS, using Scienta 200U and Scienta 100 electron analyzers, respectively. Alkali metal deposition on sample surfaces is made possible with a SAES-getters cesium (Cs) deposition source attached to the main analyzing chamber of the APPLE-PGM beamline, as well as a SAES-getters potassium (K) deposition source attached to the main analyzing chamber of Beamline 12.0.1 of the ALS. We use an electric current of 5.4 (5.5) A for the Cs (K) source, which corresponds to a deposition rate of about 1 (1.3) Å/min. Samples were cleaved *in situ* under a vacuum condition better than 4×10^{-11} torr at all beamlines.

Although the zinc-blende crystal structure results in relatively rough cleaving surfaces, our HgTe crystals are found to contain a single domain, giving rise to sharp energy bands in the ARPES maps. Measurement temperatures are kept at 10–20 K. Samples are found to be stable and without degradation for a typical measurement period of 2 days. No charging effect due to insulating behavior was found for all (~ 20) samples measured.

The scanning tunneling microscopy (STM) experiments were performed on an Omicron low temperature STM system. The samples were cleaved inside the vacuum chamber. The sample temperature was kept at 78 K during the experiments.

First-principles calculations of the HgTe bulk electronic structure [Fig. 2(e)] were performed using HGH-type pseudopotentials [36] and a plane-wave basis set. The main program employed was developed by the ABINIT group [37,38]. Spin-orbit coupling was included, where appropriate, using the relativistic LDA approximation. First-principles calculations for the surface state spin polarization [Fig. 5(d)] and the surface gap [Figs. 6(a)–6(b)] are based on the local density approximation (LDA) [39] using the projector augmented wave method [40] as implemented in the VASP package [41]. The HgTe surface was simulated by a slab with a thickness of 55 layers and the vacuum thickness larger than 15 Å. The electronic structures were optimized using a $9 \times 6 \times 1$ Monkhorst-Pack k point, and the atomic positions near the surface were relaxed until the residual forces were less than 0.01 eV/Å. The spin-orbit coupling was included self-consistently in the electronic structure calculations.

To theoretically investigate the “surface insulating gap” of as-grown HgTe single crystals (last part of Sec. IV), a *slab* calculation (detailed above) is first performed to determine the lattice relaxation of the surface layers by limiting the residual forces to 0.01 eV/Å. Another *bulk* band calculation (detailed above) is performed after the slab calculation, taking the lattice relaxation into account. The result of this two-step calculation is valid only for the surface layers of as-grown HgTe crystals and for the estimation of the gap size before deposition.

III. CRYSTAL STRUCTURE, BRILLOUIN ZONE, AND EXPERIMENTAL CHARACTERIZATION OF THE CLEAVAGE PLANE

Before presenting our main experimental results, we prove here that the (110) plane is the natural cleavage plane of HgTe. Firstly, this is done by comparing the Laue diffraction pattern measured on our samples [Fig. 1(a)] and the electron diffraction pattern obtained by transmission electron microscopy (TEM) on a standard (110) plane (Fig. 1(b), Ref. [42]). It is clear from Fig. 1 that the main diffraction peaks in the Laue and TEM results have one to one correspondence, marked by a dashed square and labels of two main bright spots in both panels. Ratio of edge lengths of the dashed squares measured $1 : \sqrt{2}$, which matches the x - y atomic distance ratio for the (110) plane of a zinc-blende structure. Secondly, the (110) cleaving plane is observed directly by atomic resolved STM images [Figs. 1(c) and 1(d)]. Direct measurements of the distances between surface atoms resolved in the 7×7 nm² STM image reveal that $d_x = a$ and $d_y = \sqrt{2}a$, matching

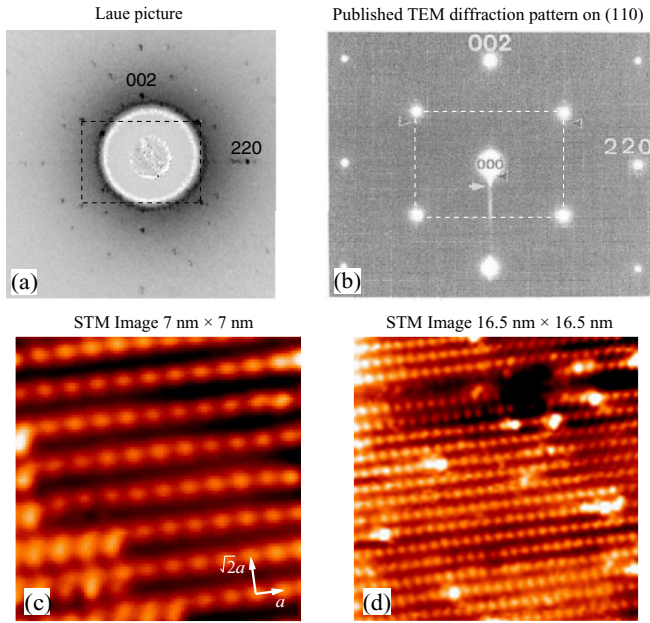


FIG. 1. (Color online) Characterization of the HgTe cleavage plane. (a) A typical Laue diffraction pattern of our HgTe samples. (b) Standard (110) electron diffraction pattern of HgTe measured by transmission electron microscopy (TEM). Figure duplicated from Ref. [42]. The one-to-one correspondence of the diffraction peaks proves that our samples cleave along the (110) plane. (c) A 7 nm \times 7 nm STM image of the HgTe (110) surface taken at $V = +2.0$ V and $I = 50$ pA. (d) A 16.5 nm \times 16.5 nm STM image of the HgTe (110) surface taken at $V = +2.0$ V and $I = 50$ pA. The 1 : $\sqrt{2}$ ratio of the x - y lattice constant as well as the lattice separation $a = 6.46$ Å proves that our samples cleave along the (110) plane.

perfectly with the (110) plane characteristics. Therefore the (110) cleaving plane of HgTe is proven without ambiguity.

Figures 2(a) and 2(b) present the zinc-blende face centered cubic (*fcc*) crystal structure and the corresponding Brillouin zone, where the (110) plane is selected as the top plane. Arrangement of the Hg and Te atoms (red and blue balls, respectively) proves that this system is noncentrosymmetric, lacking the spatial inversion symmetry. The corresponding Brillouin zone of this setup is shown in Fig. 2(b), where the bulk, *fcc* Brillouin zone of HgTe is rotated such that the W - K - W segment is parallel to the k_x axis, and that the K - X - W square is perpendicular to the k_y axis. The surface Brillouin zone is marked by four \bar{S} points which are the W and L points projected to the k_x - k_y plane [(110) plane], forming a rectangle with dimensions $(\pi/a, \sqrt{2}\pi/a)$ [red rectangle in Fig. 2(b)]. Note that the projected bulk Brillouin zone in the k_x - k_y plane has a different shape than that in the k_x - k_z plane [(001) plane], thus electronic structure in these two planes are different.

IV. ELECTRONIC STRUCTURE OF AS-GROWN HgTe BULK CRYSTALS

Figures 2(c)–2(f) present an overlook of the surface electronic structure measured by ARPES. From the ARPES k - E map in Fig. 2(c) and constant energy stacks in Fig. 2(d), we see that the Fermi surface of (the surface layers of) bulk

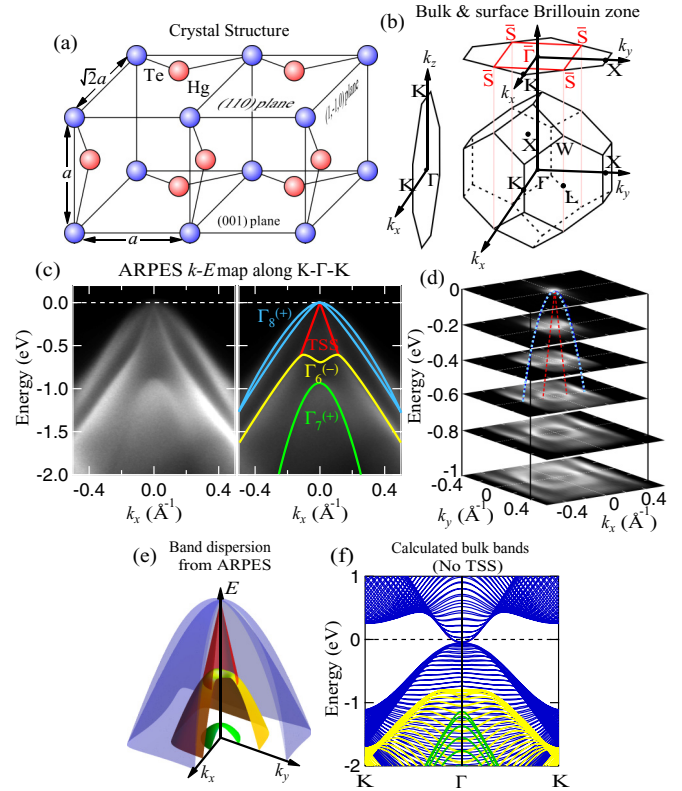


FIG. 2. (Color online) Surface electronic structure of HgTe. (a) Crystal structure of HgTe. $a = 6.46$ Å is the lattice parameter for the zinc-blende cubic cell. (b) Bulk (black) and surface (red) Brillouin zone and notations of high symmetry points. (c) ARPES k - E map along k_x (Γ - K). Left panel: raw data; right panel: raw data with dispersion of bands as guides to the eye. (+)/(-) denote the “adiabatic parity” of each energy band [17]. The M shape of the Γ_6 band represent no more than a possible dispersion consistent with our calculation in (f). (d) ARPES constant energy map stack along the k_x - k_y plane. (e) Cartoon for the band dispersion revealed from ARPES, in comparison with (f), the theoretical bulk band structure projected onto the (110) plane.

HgTe is a mere point at $\Gamma/\bar{\Gamma}$. At higher binding energies (E_B), the outer Γ_8 band forms a rectangular shape; a very sharp inner cusp-like band forms a circular contour up to $E_B \sim 0.8$ eV where it is replaced by the rectangular Γ_6 band. The reverse order of Γ_8 and Γ_6 bands as well as the switched total “adiabatic parity” [(+)/(−) in Fig. 2(c), see Ref. [25]] as compared to the non-spin-orbit-coupled calculation [17] represent the well-known topological nontriviality of HgTe. The connectivity between the Γ_8 and Γ_6 bands, the linear and isotropic (circular) dispersion, as well as the lack of k_z dispersion of the inner band (detailed later) indicate that it is a TSS of HgTe, a statement also drawn in Ref. [18]. The linewidth of the TSS is measured to be as small as ~ 0.02 Å⁻¹ (full width half maximum). Also it does not feel the rectangular symmetry of the bulk Brillouin zone, as it remains circular in shape up to $E_B \sim 0.8$ eV. These properties are consistent with the surface origin of the inner, Λ -shaped band. In Fig. 2(f), we present the *ab initio* bulk band structure projected onto the (110) surface, which is consistent with state-of-the-art

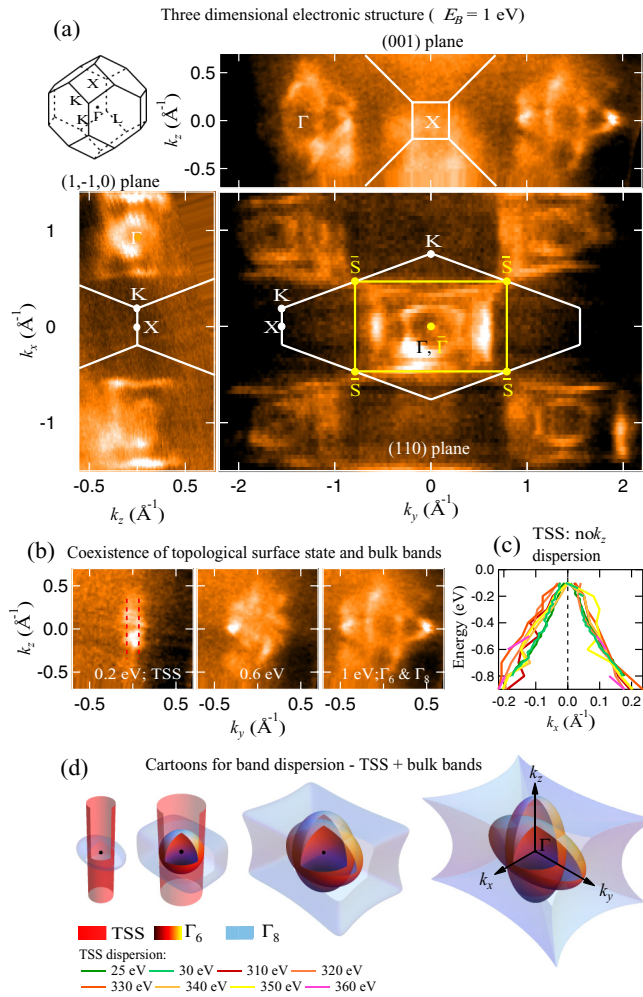


FIG. 3. (Color online) Coexistence of bulk electronic structure and two-dimensional Dirac cone. (a) Three-dimensional electronic structure of HgTe measured by soft x-ray ARPES. Band dispersion is shown at a binding energy (E_B) of 1 eV. (b) ARPES constant energy maps at different binding energies. Red lines mark the TSS. (c) Lorentzian fittings of the TSS for a large range of photon energies. (d) Cartoons for the three-dimensional band dispersion of HgTe. Binding energy increases from left to right.

GW calculations on HgTe [43,44]. No bulk band appears in the partial gap between Γ_8 and Γ_6 . These findings, taken together, serve as direct evidences that the cusp-like inner band (red) originates from the sample surface, consistent with the characteristics of a TSS. We summarize the ARPES data in Fig. 2 by presenting a cartoon showing the ARPES extracted (110) surface electronic structure in Fig. 2(e).

In Fig. 3, we study the electronic structure of HgTe across the entire 3D k space, which has not been reported with ARPES measurements albeit the heated scientific interest of this material. Data is obtained using a soft x-ray ARPES setup with photon energies ranging from 310 to 700 eV (raw data shown in Fig. 4). Experimental geometry is given in Ref. [45]. Figure 3(a) presents the ARPES constant energy maps at $E_B = 1$ eV for the three high-symmetry cross-sections of the k space. At this binding energy, the TSS is replaced by the bulk Γ_6 band; all bands seen by ARPES are thus highly dispersive

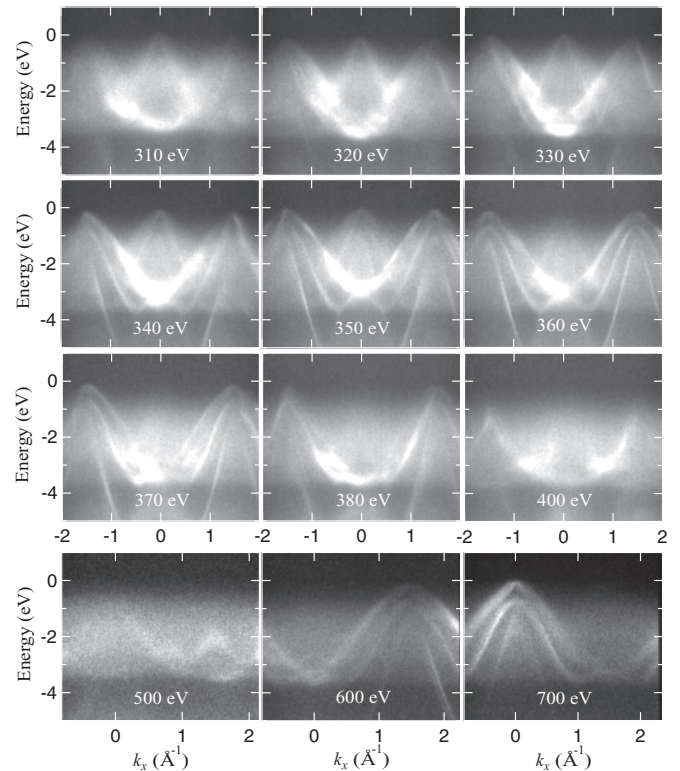


FIG. 4. Soft x-ray ARPES $k - E$ maps of HgTe at photon energies $310 < h\nu < 700$ eV [raw data for Fig. 3(c)]. k_z dispersion on the TSS is negligible. The TSS is not visible for $370 < h\nu < 600$ eV because of near-vanishing matrix element for this state.

along k_z . As the binding energy decreases, ARPES intensity of the TSS becomes dominant, and non- k_z -dispersive state is expected close to $\bar{\Gamma}$. As shown in Fig. 3(b), at $E_B = 0.2$ eV, the resolved band experiences significant elongation along the k_z axis. Since k_z is equivalent to k_y in the bulk Brillouin zone [both are (110) directions], such elongation can only be explained by the existence of a 2D surface state that appears at lower binding energies. The non- k_z -dispersive nature of the TSS is further emphasized in Fig. 3(c) where its band dispersion is extracted for a large photon energy (k_z) range (25 to 360 eV). We see clearly that the TSS shows no k_z dispersion within experimental error. The TSS is not visible in ARPES spectra from 370 to 420 eV (Fig. 4) due to highly suppressed photoemission matrix element value. To summarize, we draw in Fig. 3(d) cartoons of the experimentally deduced constant energy band contours in three dimensions. The TSS of HgTe forms a cylinder whose radius increases with binding energy; the bulk Γ_8 and Γ_6 bands form complicated holelike contours that dominates the ARPES intensity at high E_B 's. With the help of more bulk sensitive soft x-ray ARPES, the complete electronic structure of HgTe is measured for the first time.

In Fig. 4, we show the raw ARPES data of Fig. 3(c), together with soft x-ray ARPES k - E maps measured with an even larger photon energy range: $310 < h\nu < 700$ eV. Due to soft x-ray photon energy and usage of the wide angular mode (WAM) at the ADDRESS beamline [23], three Brillouin zones are visible in a single k - E map for photon energies from 310 to 400 eV. From, e.g., the 360 eV map, one sees

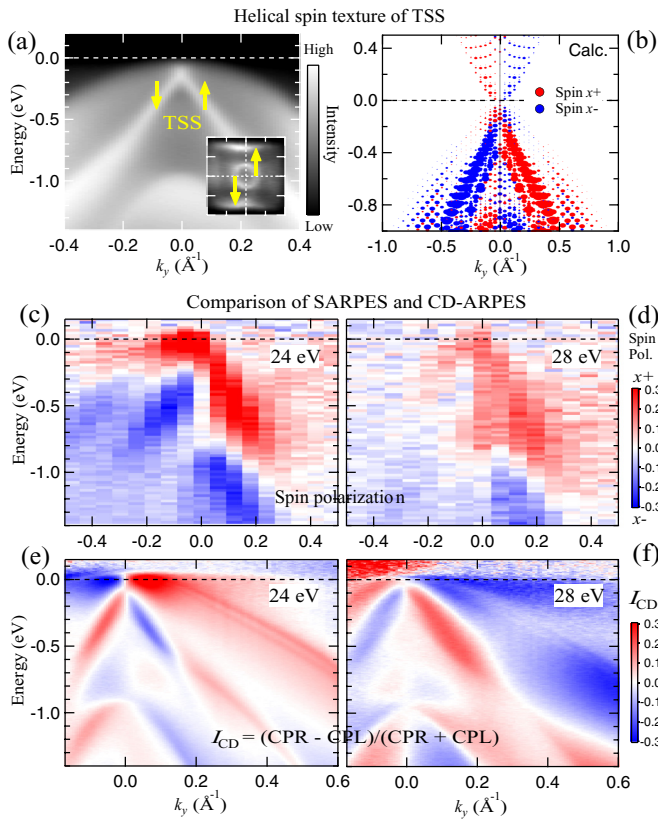


FIG. 5. (Color online) Spin polarization and dichroism of the topological surface state. (a) ARPES k - E map along k_y (Γ - X), revealing the topological surface state (TSS). (Inset) ARPES constant energy map at 600-meV binding energy. Yellow arrows mark the spin helical texture of the TSS. (b) Spin helical texture of the TSS obtained by first-principles slab calculation (detailed in text), showing excellent consistency with SARPES results in (c) and (d). (c) and (d) Spin-resolved ARPES data along k_y measured with (c) 24- and (d) 28-eV photons, showing the spin polarization tangential to the TSS (i.e., s_x). (e) and (f) CD-ARPES data along k_y measured with (e) 24- and (f) 28-eV photons.

that three bulk bands, Γ_8 (lower portion), Γ_6 and Γ_7 from low to high binding energies, are clearly visible for the left and right zones. These bulk bands are k_z dispersive as seen from panels of 370–400 eV photon energies. At 370 eV, the lower portion of Γ_8 touches E_F , whereas at 400 eV it lowers to ~ 1 eV binding energy. Γ_6 and Γ_7 follows basically the same trend. The Λ -shaped TSS is resolved in the first Brillouin zone (central zone), which is more clearly visible in photon energy range of 310–350 eV. The TSS is not visible in ARPES spectra from 370 to 500 eV due to highly suppressed photoemission matrix element value. Together with Fig. 3, the complete three-dimensional electronic structure of HgTe and its coexistence of the two-dimensional TSS is studied comprehensively.

Spin resolved (S) and circular dichroic (CD) ARPES mappings shown in Fig. 5 present the critical and unambiguous proof that the inner band is a TSS of HgTe, and that large spin polarization of the TSS persists within the bulk band continuum. Figure 5(a) shows the spin integrated ARPES data with spin polarization obtained from Figs. 5(c) and 5(f). The spin polarization maps [Figs. 5(c) and 5(d)], achieved using

the VLEED spin detection technique (see Ref. [25]), sends out a clear message that the inner band features a right-handed spin helical texture, which is unique for a spin momentum locked TSS. Clearly, the s_{x+} quasiparticles (red) situate solely on the $+k_y$ side, whereas the s_{x-} quasiparticles (blue) situate solely on the $-k_y$ side. On the other hand, we performed first-principles slab calculation on similar energy and momentum range as in the measurements, the result of which is shown in Fig. 5(b). Firstly, the inner Λ -shaped band absent in bulk calculation [Fig. 2(f)] appears when the sample surface is taken into account. Secondly, from the comparison between Figs. 5(b) and 5(c), a remarkable consistency is found for the strong spin helical behavior between the calculational and experimental results. The conclusive observation in Figs. 5(b)–5(d) thus proves that the inner Λ -shaped band that appears in the (110) surface electronic structure of HgTe is (the lower part of) a Dirac cone TSS whose Dirac point is very close to the as-cleave Fermi level. Note that a spin-polarization signal is present also in bulk states such as Γ_7 ($E_B \sim 0.8$ eV). This signal appears both in the SARPES measurements and theoretical calculations [Figs. 5(b)–5(d)]. Although the origin of this signal is not known, it does not affect our conclusion that the inner band is a TSS of HgTe. The degree of TSS spin polarization is found to reach about $\pm 30\%$, comparable with that found in the in-gap TSSs of prototypical TIs (e.g., Bi_2Se_3). This behavior closely resembles the spin polarized TSS found in strained α -Sn films [46,47], demonstrating that the existence of spin helical Dirac fermions is a general property in these systems.

Figures 5(e) and 5(f) show the CD-ARPES data in two different incident photon energies, 24 and 28 eV, in comparison with the SARPES maps under the same photon energy [Figs. 5(c) and 5(d)]. Two facts are worth noticing from this comparison. First, the $-k \rightarrow +k$ sign change of spin polarization is reproduced in the CD-ARPES data, which supports the statement that I_{CD} of a TSS is proportional to the quasiparticle spin. Second, the overall sign change between $I_{CD}(24 \text{ eV})$ and $I_{CD}(28 \text{ eV})$ for all resolved bands is *not* reproduced in the SARPES data. Such a sign change relates to a sign-changing modulation of the orbital angular momentum (OAM) rather than the physical spin. Despite the more complex origin of the CD-ARPES signal, the *relative* $-k \rightarrow +k$ sign change in the CD-ARPES signal still signifies the spin helical texture of the TSS, regardless of the relative intensity and handedness. We will explain the data in Fig. 7 using this argument.

Before going into the data on carrier-deposited HgTe surfaces, we would like to discuss the possibility that a full, insulating band gap between the upper and lower Γ_8 band opens in the surface layer of as-grown HgTe crystals. Our first-principles calculations as well as local density of states (LDOS) measured with dI/dV curve (STS) do not contradict to the idea that such “surface insulating gap” may exist even in as-cleaved surfaces of 3D HgTe. The evidences are listed in Fig. 6. In Fig. 6(a), we present the theoretical slab model used to calculate the surface atomic structure of HgTe. It is the same model as used in Fig. 5 for calculating the spin polarization of the TSS. We notice, as marked in Fig. 6(a), that the sample-vacuum interfacial potential barrier gives rise to a distortion of the surface atoms, under which the Hg-Te bond angle becomes 38° with respect to the surface, a phenomenon similar to the

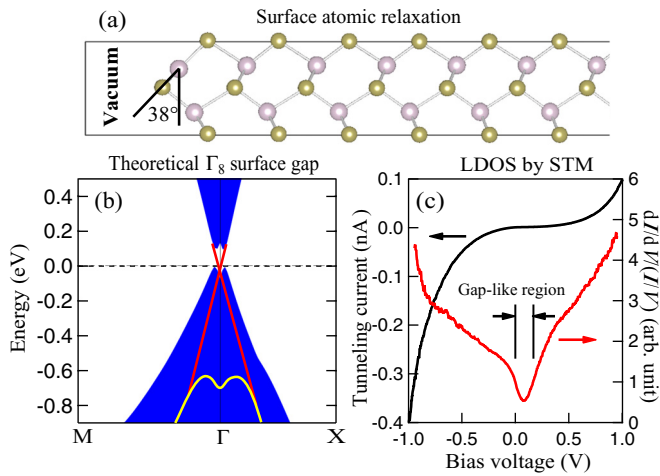


FIG. 6. (Color online) Calculational and experimental evidence for the Γ_8 gap at the HgTe surface before deposition. (a) Model and results of the first-principles slab calculation. A 55-layer-thick slab and a vacuum region thicker than 15 \AA is used (see the “Methods” section). Surface termination gives rise to a distorted 38° bond angle. (b) Results of the subsequent *bulk* band calculation, where the surface relaxation (38° bond angle tilting) is taken into account. An insulating gap opens between the $\Gamma_8^{(+)}$ and $\Gamma_8^{(-)}$ bulk bands due to the surface relaxation. Fermi level is found to touch the top of the $\Gamma_8^{(+)}$ band. Red and yellow curves (guides to the eye) indicate the TSS and the Γ_6 band, respectively. Note: the Γ_8 bulk bands appear to be solid blue because *these are results from a bulk calculation, not a slab calculation*. (c) Typical I - V (black) and $dI/dV/(I/V)$ (red) curves taken by STM on HgTe (110) surface. The set point is $V = -0.5 \text{ V}$ and $I = 50 \text{ pA}$. Local density of states (LDOS) are found to form a dip at the theoretical gap region. Nonzero LDOS inside the gap due possibly to the TSS.

distortion observed in semiconducting GaAs [48,49]. If we introduce such lattice relaxation (result of the slab calculation) into a subsequent *bulk* band calculation, we observe that a bulk insulating gap of size $\sim 100 \text{ meV}$ appears between the bulk $\Gamma_8^{(+)}$ and $\Gamma_8^{(-)}$ band [see Fig. 2(c) for band definition]. Please note that the Γ_8 bulk bands appear to be solid blue in Fig. 6(b), solely because *these are results from a bulk calculation, not a slab calculation*. In other words, electronic states appear everywhere within the Γ_8 band. However, one must keep in mind that *such calculation is valid only for the surface layer of HgTe*, since the 38° tilting angle only appears there. As one goes from the surface layers to the bulk layers, the tilting angle is expected to decrease and finally goes to zero, so the “surface gap” is expected to be suppressed and eventually vanishes in deep bulk. Note that, according to the calculation, the depth of this surface region (in which the tilting angle is finite) is greater than the 55 layers we used in our calculation model as well as the ARPES penetration depth. In Fig. 6(c), we present a typical $dI/dV/(I/V)$ curve (STS) taken on the clean (110) surface of 3D HgTe, which is believed to be proportional to the LDOS [50]. A rapid decrease and increase of $dI/dV/(I/V)$ sitting just above the Fermi level is revealed, which shows no contradiction to the existence of a gaplike feature in the energy bands of size $\sim 150 \text{ meV}$. Both the location and the size coincides with the theoretical prediction very nicely, except

that the experimental observed gap is not a full gap but is partially filled. Since the sample temperature was kept at 78 K during the experiments, thermal broadening is not sufficient to fill this relatively wide gap. Therefore it is likely caused by the contributions from the TSS (if the probing depth of STS is smaller than the penetration depth of the gap). In conclusion, theoretical and experimental results do not contradict to the existence of a Γ_8 insulating gap as large as $100\text{--}150 \text{ meV}$ near the surface of 3D HgTe crystals. Although other explanations for the dI/dV dip cannot be ruled out, it is possible that a true insulating gap exists at the surfaces of 3D HgTe, resulting in a surface-bound topological *insulating* state which have not been observed in any topological semimetal.

V. ELECTRONIC STRUCTURE OF HgTe UNDER SURFACE DEPOSITION

From the previous section, we deduced that the surface layer of 3D HgTe is possibly a fully gapped topological insulator with a single Dirac cone topological surface state. To further investigate such an unusual state and its band structure in the unoccupied side, we examine in Fig. 7 the surface electronic states of HgTe *under alkali metal deposition* on the (110) surface. This measurement leads to a very important observation—we found a direct insulating gap hundreds of meV in size, and a fully exposed Dirac cone TSS spanning across this gap. While evidences point to the existence of an insulating gap in as-grown HgTe surfaces, the deposited surface of a HgTe single crystal is *proved* to exhibit all spectroscopic signatures for a 3D topological insulator. In Figs. 7(a)–7(e), we present the ARPES k - E maps under increasing cesium dosage which n dopes the system. The crucial observation is that a V-shaped band [dashed lines in Fig. 7(e)] becomes visible as E_F raises, combining with the Λ -shaped TSS to form a perfect X-shaped, linearly dispersive band across the topologically nontrivial gap between Γ_6 and the upper portion of Γ_8 [visible in Fig. 7(k)]. The topological nature of this X-shaped band is revealed in Figs. 7(f)–7(j) where we perform CD-ARPES measurements on the deposited surface. For the upper portion of the X band, the CD signal shows clear left-right imbalance and a reversed sign with respect to the lower portion. Using the argument we drawn for CD-ARPES signal in Fig. 5, we conclude that this X-shaped band is a true gapless Dirac cone TSS. The finite in-gap density of states results solely from this TSS. Topological transport behavior is expected in a large energy range across E_F , and at certain deposition levels [e.g., Figs. 7(b) and 7(c)] only the TSS is found to cross E_F , realizing a bulk *insulator* at least from the ARPES point of view. In Fig. 7(k), we measured the electronic structure under increasing *potassium* dosage. Not only does high K deposition reproduces the upper Dirac cone seen with surface Cs dopants, the bottom of the bulk conduction band (upper portion of Γ_8) also becomes visible. Interestingly, the gap size is found to increase with increasing potassium deposition, from about 290 meV at 2 \AA K dosage, to about 392 meV at 3.3 \AA K dosage [Fig. 7(l)]. From the data in Fig. 7, the topological insulating nature of the HgTe surface deposited with alkali metals is proven without ambiguity.

In Fig. 8, we investigate the time evolution of the electronic structure in the deposited surface, showing that this electron

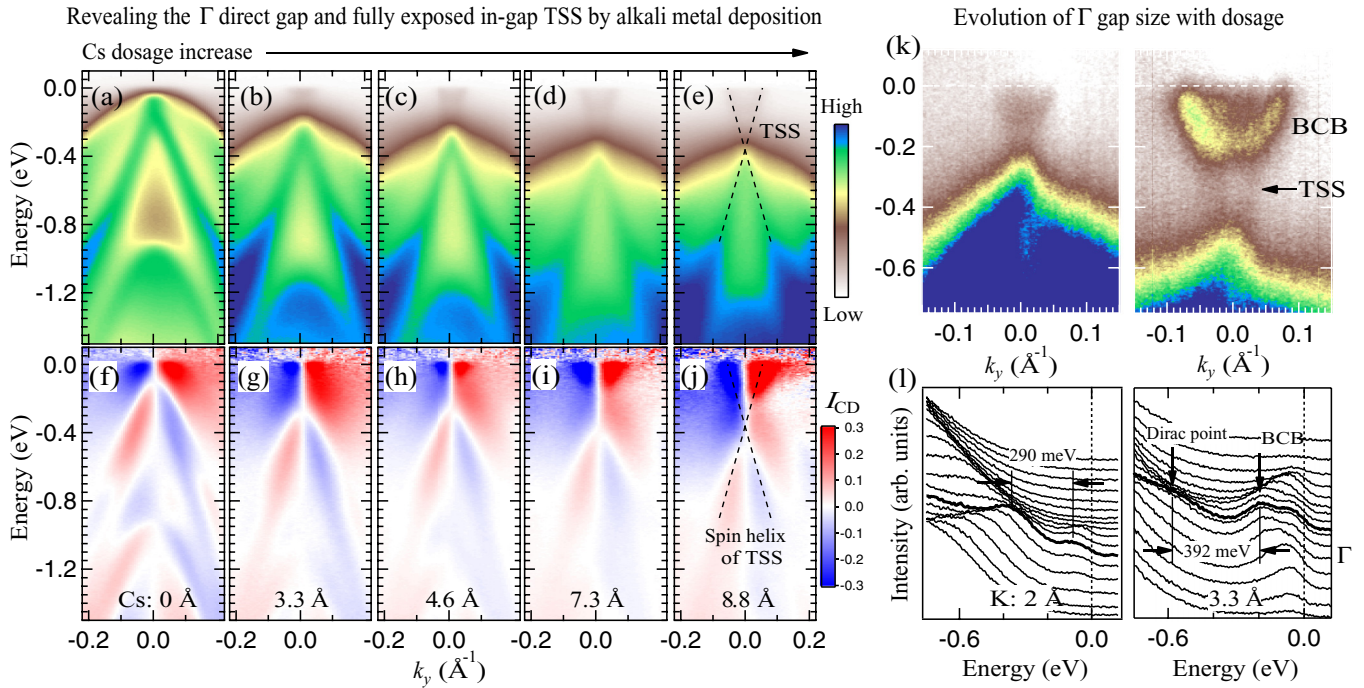


FIG. 7. (Color online) Surface insulating gap and full exposure of Dirac cone revealed by alkali metal deposition. (a)–(e) ARPES k - E maps under increasing Cs deposition. (f)–(j) CD-ARPES k - E maps under the same Cs dosage (estimated Cs deposition rate: 1 Å/min). Black dashed lines in (e) and (j) mark the linear dispersion of the TSS. (k)–(l) Evolution of full insulating gap under surface K deposition. Gap size increases from 290 to 392 meV with increasing K dosage (K deposition rate: 1.3 Å/min).

doped state is not stable over time. At a relatively low temperature ($T = 12$ K), the increased electron concentration from alkali metal deposition gradually retracts; within hours the HgTe surface returns to the electron-hole balanced situation where the Fermi level lies ~ 50 meV above the Dirac point. We demonstrate this process in Fig. 8 where the same ARPES k - E map is taken repeatedly under increasing Cs dosage, except for panels 3 and 4 who are taken 12 hours apart but with no additional Cs deposition. When the ARPES maps are taken not-so-long (within 30 min) between one another, a gradual increase of electron concentration leads to an apparent upturn

of the Fermi level (panels 1–3 and 4–7), showing that the Cs adatoms contribute extra electrons to the HgTe surface. However, when we let the samples sit at 12 K in ultrahigh vacuum for an extended period of time (in this case 12 hours, panel 3 \rightarrow 4), the degree of electron doping retracts abruptly; the Fermi energy returns almost to the as-cleave level— ~ 50 meV above the Dirac point. Therefore the deposited surface is not stable over time, the reason of which is likely that the extra electron situating at the surface are gradually absorbed by the crystal bulk, moving to a depth where photoemission is unable to detect. Note that the same

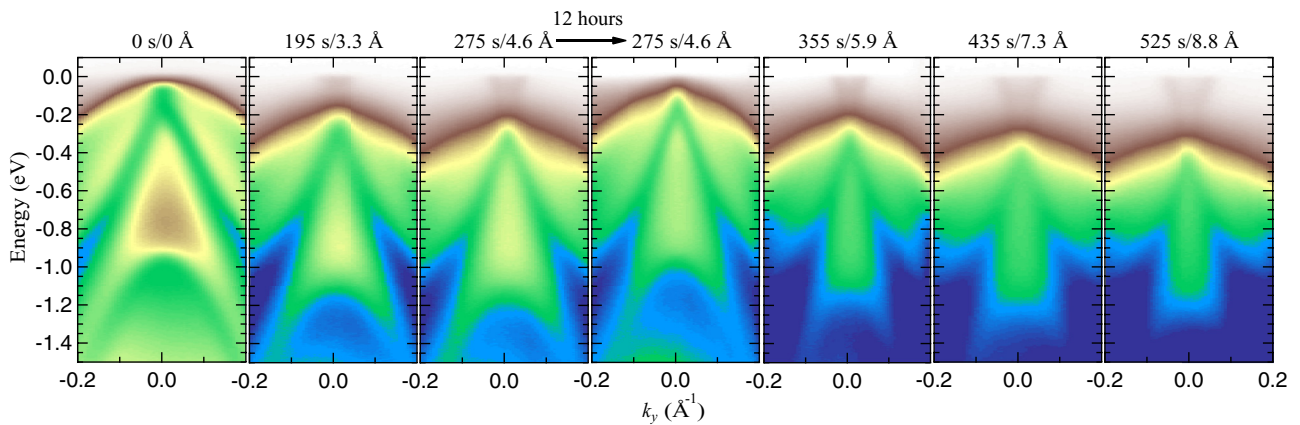


FIG. 8. (Color online) Instability of the Cs deposited HgTe (110) surface. The deposition is done at $T = 12$ K. Left to right: ARPES k - E maps for the HgTe surface under increasing Cs dosage. Filament current of the Cs deposition source is 5.4 A. Numbers on top of each panel mark the integrated deposition time and the estimated Cs dosage using a deposition rate of 1 Å/min. Data acquisition is separated by 12 hours between panels 3 and 4. Clearly, the electron doping retracts drastically over time, i.e., the deposited surface is unstable.

deposition process is also performed at room temperature (data not shown). In this case, the Fermi level is retracting so quickly back to the as-grown level such that no increase of electron count could be seen, neither does the upper portion of the Dirac cone TSS or the BCB; the k - E map appears to be not changing at all. In order to realize a stable surface three-dimensional TI state, we thus need to seek for a stable *bulk* electron dopant instead of surface deposition. Needless to say, alkali metal doped HgTe is a promising candidate.

The unexpected results shown in Figs. 6(c), 7, and 8 warrants further discussion. So far, we have made theoretical arguments for a nonvanishing gap (100–150 meV in size) at the as-cleaved HgTe (110) surface; our ARPES and STS data show no contradiction to this argument. More importantly, a solid proof is presented for the existence and monotonic increase of such a gap in surfaces deposited by alkali metals, up to ~ 400 meV at high dosage. In other words, if we plotted the gap size (either hypothesized or proved) as a function of K dosage, we would see an almost linear trend of gap increase under increasing dosage. If we extrapolate linearly the gap values [$\Delta(2) = 290$ meV, $\Delta(3.3) = 392$ meV] for the K deposited surface back to zero dosage, we would obtain $\Delta(0) = 140$ meV, consistent with both the theoretical value (~ 100 meV) and the STS data (~ 150 meV, although one can debate whether or not the STS actually shows the gap). Therefore the most likely picture here is that this surface gap exists intrinsically, and can also be modulated by surface deposition. Staying in ultrahigh vacuum causes a retraction of the doping effect, while further increase of dosage compensates such retraction. These treatments create together a recipe to accurately control the Fermi level and the surface gap size of 3D HgTe. Such surface semimetal-to-TI transition and the accurate gap control is thus far unseen in any topological system.

As for the origin of the surface gap, here we introduce an idea which is consistent with our data, without ruling out other possibilities. Crystallographic symmetry of HgTe requires a vanishing gap for the bulk bands [17,51], but a complete insulating gap in the order of 300 meV can be introduced in the surface layers where the lattice constant ratio a/c can be different from the bulk value [$(a/c)_{\text{bulk}} = 1$] (Ref. [22]). The farther the a/c ratio is away from unity, the larger the gap. In our experiment, when the surface is deposited by alkali atoms, as more adatoms are introduced to the surface, the scale of the surface relaxation enlarges, thus the gap also increases. If one examines Figs. 7(a)–7(e) with greater care, it may be noticed that there is extra intensity near the Fermi level, which could be attributed to the bulk state, just as in the case of K deposition [Fig. 7(k)], although an unambiguous demonstration of this would need careful analysis of the EDCs and MDCs. Please note, however, that even if such extra intensity was indeed due to the bulk conduction band, our main conclusion on the insulating gap—that it is larger than

100 meV and is increasing with increasing dosage—remains valid. On the other hand, effects from charge accumulation layer [2] may result in seemingly alike ARPES observations, but this does not affect the main conclusions of the paper that a controlled deposition/aging sequence provides accurate manipulation on the Fermi level and the surface gap size of 3D HgTe. Taken collectively, our comprehensive study on 3D HgTe paves the way for a convenient control of the Fermi surface and quantum transport in a topological insulator, which is extremely important for future mass production of functional TI materials. This study also sheds light on future spectroscopic and transport research on this topologically nontrivial system with a spin splitting of bulk bands, laying the foundation for realizing noncentrosymmetric topological phenomena in future devices.

ACKNOWLEDGMENTS

Work at Princeton and Princeton-led synchrotron-based measurements and the related theory at Northeastern University are supported by the Office of Basic Energy Sciences, US Department of Energy (grants DE-FG-02-05ER46200, AC03-76SF00098 and DE-FG02-07ER46352), and benefited from the allocation of supercomputer time at NERSC and Northeastern University's Advanced Scientific Computation Center. STM measurements are supported by the Research Grants Council of Hong Kong (Grant No. 404613) and the National Basic Research Program of China (973 Program) under Grant No. 2014CB921402. Crystal growth at Purdue University is supported by DARPA-MESO program (grant No. N66001-11-1-4107). Spin resolved ARPES experiments were performed with the approval of Hiroshima Synchrotron Radiation Center. Soft x-ray ARPES experiments were performed at the ADDRESS beamline of the Swiss Light Source. The Advanced Light Source is supported by the Director, Office of Science, Office of Basic Energy Sciences, of the U.S. Department of Energy under Contract No. DE-AC02-05CH11231. The Stanford Synchrotron Radiation Lightsource is supported by the U.S. Department of Energy under Contract No. DE-AC02-76SF00515. The Synchrotron Radiation Center is primarily funded by the University of Wisconsin-Madison with supplemental support from facility users and the University of Wisconsin-Milwaukee. We gratefully thank Sung-Kwan Mo, Jonathan D. Denlinger and Donghui Lu for instrumental support. C. L. acknowledges Takeshi Kondo and Adam Kaminski for provision of data analysis software. H. L. acknowledges the Singapore National Research Foundation for support under NRF Award No. NRF-NRFF2013-03. T. O. acknowledges the financial support by JSPS KAKENHI Grant No. 23244066. M. Z. H. acknowledges Visiting Scientist support from LBNL and additional support from the A. P. Sloan Foundation.

[1] K.-U. Gawlik, L. Kipp, M. Skibowski, N. Orłowski, and R. Manzke, *Phys. Rev. Lett.* **78**, 3165 (1997).
 [2] T. Dietl, W. Dobrowolski, J. Kossut, B. J. Kowalski, W. Szuszkiewicz, Z. Wilamowski, and A. M. Witowski, *Phys. Rev. Lett.* **81**, 1535 (1998).

[3] N. Orłowski, J. Augustin, Z. Gołacki, C. Janowitz, and R. Manzke, *Phys. Rev. B* **61**, R5058 (2000).
 [4] C. Janowitz, N. Orłowski, R. Manzke, and Z. Gołacki, *J. Alloys Comp.* **328**, 84 (2001).

- [5] M. König, S. Wiedmann, C. Brüne, A. Roth, H. Buhmann, L. W. Molenkamp, X.-L. Qi, and S.-C. Zhang, *Science* **318**, 766 (2007).
- [6] M. Z. Hasan and C. L. Kane, *Rev. Mod. Phys.* **82**, 3045 (2010).
- [7] X.-L. Qi and S.-C. Zhang, *Rev. Mod. Phys.* **83**, 1057 (2010).
- [8] J. E. Moore, *Nature (London)* **464**, 194 (2010).
- [9] L. Fu, C. L. Kane, and E. J. Mele, *Phys. Rev. Lett.* **98**, 106803 (2007).
- [10] J. E. Moore and L. Balents, *Phys. Rev. B* **75**, 121306(R) (2007).
- [11] D. Hsieh, D. Qian, L. Wray, Y. Xia, Y. S. Hor, R. J. Cava, and M. Z. Hasan, *Nature (London)* **452**, 970 (2008).
- [12] D. Hsieh, Y. Xia, D. Qian, L. Wray, J. H. Dil, F. Meier, J. Osterwalder, L. Patthey, J. G. Checkelsky, N. P. Ong, A. V. Fedorov, H. Lin, A. Bansil, D. Grauer, Y. S. Hor, R. J. Cava, and M. Z. Hasan, *Nature (London)* **460**, 1101 (2009).
- [13] Y. L. Chen, J. G. Analytis, J.-H. Chu, Z. K. Liu, S.-K. Mo, X. L. Qi, H. J. Zhang, D. H. Lu, X. Dai, Z. Fang, S. C. Zhang, I. R. Fisher, Z. Hussain, and Z.-X. Shen, *Science* **325**, 178 (2009).
- [14] D. Hsieh, Y. Xia, L. Wray, D. Qian, A. Pal, J. H. Dil, J. Osterwalder, F. Meier, G. Bihlmayer, C. L. Kane, Y. S. Hor, R. J. Cava, and M. Z. Hasan, *Science* **323**, 919 (2009).
- [15] Z.-H. Pan, E. Vescovo, A. V. Fedorov, G. D. Gu, and T. Valla, *Phys. Rev. B* **88**, 041101(R) (2013).
- [16] B. A. Bernevig, T. L. Hughes, and S.-C. Zhang, *Science* **314**, 1757 (2006).
- [17] L. Fu and C. L. Kane, *Phys. Rev. B* **76**, 045302 (2007).
- [18] C. Brüne, C. X. Liu, E. G. Novik, E. M. Hankiewicz, H. Buhmann, Y. L. Chen, X. L. Qi, Z. X. Shen, S. C. Zhang, and L. W. Molenkamp, *Phys. Rev. Lett.* **106**, 126803 (2011).
- [19] K. Ishizaka, M. S. Bahramy, H. Murakawa, M. Sakano, T. Shimojima, T. Sonobe, K. Koizumi, S. Shin, H. Miyahara, A. Kimura, K. Miyamoto, T. Okuda, H. Namatame, M. Taniguchi, R. Arita, N. Nagaosa, K. Kobayashi, Y. Murakami, R. Kumai, Y. Kaneko, Y. Onose, and Y. Tokura, *Nat. Mater.* **10**, 521 (2011).
- [20] G. Landolt, S. V. Eremeev, Y. M. Koroteev, B. Slomski, S. Muff, T. Neupert, M. Kobayashi, V. N. Strocov, T. Schmitt, Z. S. Aliev, M. B. Babanly, I. R. Amiraslanov, E. V. Chulkov, J. Osterwalder, and J. H. Dil, *Phys. Rev. Lett.* **109**, 116403 (2012).
- [21] H. Murakawa, M. S. Bahramy, M. Tokunaga, Y. Kohama, C. Bell, Y. Kaneko, N. Nagaosa, H. Y. Hwang, and Y. Tokura, *Science* **342**, 1490 (2013).
- [22] H. Han, Y. Zhang, G. Y. Gao, and K. L. Yao, *Solid State Commun.* **153**, 31 (2013).
- [23] V. N. Strocov, T. Schmitt, U. Flechsig, T. Schmidt, A. Imhof, Q. Chen, J. Raabe, R. Betemps, D. Zimoch, J. Krempasky, X. Wang, M. Grioni, A. Piazzalunga, and L. Patthey, *J. Synchrotron Rad.* **17**, 631 (2010).
- [24] T. Okuda, K. Miyamaoto, H. Miyahara, K. Kuroda, A. Kimura, H. Namatame, and M. Taniguchi, *Rev. Sci. Instrum.* **82**, 103302 (2011).
- [25] See Supplemental Material at <http://link.aps.org/supplemental/10.1103/PhysRevB.92.115436> for explanation of “adiabatic parity” and details of the VLEED spin detection technique.
- [26] A. A. Soluyanov and D. Vanderbilt, *Phys. Rev. B* **83**, 235401 (2011).
- [27] C. Bouvier, T. Meunier, P. Ballet, X. Baudry, R. B. G. Kramer, and L. Lévy, [arXiv:1112.2092](https://arxiv.org/abs/1112.2092).
- [28] T. Okuda, Y. Takeichi, Y. Maeda, A. Harasawa, I. Matsuda, T. Kinoshita, and A. Kakizaki, *Rev. Sci. Instrum.* **79**, 123117 (2008).
- [29] E. Kisker, R. E. Kirby, E. L. Garwin, F. K. King, E. Tamura, and R. Feder, *J. Appl. Phys.* **57**, 3021 (1985).
- [30] E. Tamura, R. Feder, J. Krewer, R. E. Kirby, E. Kisker, E. L. Garwin, and F. K. King, *Solid State Commun.* **55**, 543 (1985).
- [31] Th. Dodt, D. Tillmann, R. Rochow, and E. Kisker, *Europhys. Lett.* **6**, 375 (1988).
- [32] A. Winkelmann, D. Hartung, H. Engelhard, C.-T. Chiang, and J. Kirschner, *Rev. Sci. Instrum.* **79**, 083303 (2008).
- [33] F. Meier, J. H. Dil, and J. Osterwalder, *New J. Phys.* **11**, 125008 (2009).
- [34] T. Okuda and A. Kimura, *J. Phys. Soc. Jpn.* **82**, 021002 (2013).
- [35] C. Jozwiak, C.-H. Park, K. Gotlieb, C. Hwang, D.-H. Lee, S. G. Louie, J. D. Denlinger, C. R. Rotundu, R. J. Birgeneau, Z. Hussain, and A. Lanzara, *Nat. Phys.* **9**, 293 (2013).
- [36] C. Hartwigsen, S. Goedecker, and J. Hutter, *Phys. Rev. B* **58**, 3641 (1998).
- [37] X. Gonze, J.-M. Beuken, R. Caracas, F. Detraux, M. Fuchs, G.-M. Rignanese, L. Sindic, M. Verstraete, G. Zerah, F. Jollet, M. Torrent, A. Roy, M. Mikami, P. Ghosez, J.-Y. Raty, and D. C. Allan, *Comp. Mater. Sci.* **25**, 478 (2002).
- [38] X. Gonze, G.-M. Rignanese, M. Verstraete, J.-M. Beuken, Y. Pouillon, R. Caracas, F. Jollet, M. Torrent, G. Zerah, M. Mikami, Ph. Ghosez, M. Veithen, J.-Y. Raty, V. Olevano, F. Bruneval, L. Reining, R. W. Godby, G. Onida, D. R. Hamann, and D. C. Allan, *Z. Kristallogr.* **220**, 558 (2005).
- [39] D. M. Ceperley and B. J. Alder, *Phys. Rev. Lett.* **45**, 566 (1980).
- [40] P. E. Blöchl, *Phys. Rev. B* **50**, 17953 (1994); G. Kresse and D. Joubert, *ibid.* **59**, 1758 (1999).
- [41] G. Kresse and J. Hafner, *Phys. Rev. B* **48**, 13115 (1993); G. Kresse and J. Furthmüller, *Comput. Mater. Sci.* **6**, 15 (1996); *Phys. Rev. B* **54**, 11169 (1996).
- [42] X. F. Zhang, C. R. Becker, H. Zhang, L. He, and G. Landwehr, *Semicond. Sci. Technol.* **9**, 2217 (1994).
- [43] R. Sakuma, C. Friedrich, T. Miyake, S. Blügel, and F. Aryasetiawan, *Phys. Rev. B* **84**, 085144 (2011).
- [44] A. Svane, N. E. Christensen, M. Cardona, A. N. Chantis, M. van Schilfgaarde, and T. Kotani, *Phys. Rev. B* **84**, 205205 (2011).
- [45] V. N. Strocov, X. Wang, M. Shi, M. Kobayashi, J. Krempasky, C. Hess, T. Schmitt, and L. Patthey, *J. Synchrotron Rad.* **21**, 32 (2014).
- [46] A. Barfuss, L. Dudy, M. R. Scholz, H. Roth, P. Höpfner, C. Blumenstein, G. Landolt, J. H. Dil, N. C. Plumb, M. Radovic, A. Bostwick, E. Rotenberg, A. Fleszar, G. Bihlmayer, D. Wortmann, G. Li, W. Hanke, R. Claessen, and J. Schäfer, *Phys. Rev. Lett.* **111**, 157205 (2013).
- [47] Y. Ohtsubo, P. Le Fèvre, F. Bertran, and A. Taleb-Ibrahimi, *Phys. Rev. Lett.* **111**, 216401 (2013).
- [48] R. M. Feenstra, Joseph A. Stroscio, J. Tersoff, and A. P. Fein, *Phys. Rev. Lett.* **58**, 1192 (1986).
- [49] S. Y. Tong, W. N. Mei, and G. Xu, *J. Vac. Sci. Technol. B* **2**, 393 (1984).
- [50] N. D. Lang, *Phys. Rev. B* **34**, 5947 (1986).
- [51] X. Dai, T. L. Hughes, X.-L. Qi, Z. Fang, and S.-C. Zhang, *Phys. Rev. B* **77**, 125319 (2008).